RSC Applied Interfaces

ROYAL SOCIETY OF CHEMISTRY

PAPER

View Article Online
View Journal | View Issue

Cite this: *RSC Appl. Interfaces*, 2024, **1**, 1020

Ex situ poly-DOL coatings for lithium metal protection†

Yifan Zhao, Sanaz Ketabi,* Manuela Ferreira, Xingcheng Xiao, Fang Dai and Mei Cai

Received 10th March 2024,
Accepted 26th April 2024

DOI: 10.1039/d4lf00083h

rsc.li/RSCApplInter

Lithium metal is a promising anode material candidate for next-generation high energy density batteries owing to its high theoretical specific capacity and low electrochemical potential. However, rapid capacity fade and safety issues due to inhomogeneous deposition and side reaction between lithium and electrolyte are the main hindrance to the successful utilization of the lithium metal anode. As a solid electrolyte interphase (SEI) plays an important role in lithium stripping and deposition, we propose a multi-component, organic–inorganic composite artificial SEI formed by ring-opening polymerization of 1,3-dioxolane (DOL) with incorporation of inorganic salt additives. The formed poly-DOL can provide a robust and flexible organic matrix which confines the reduction of other components to form a composite SEI and protect the lithium metal anode to improve the cycle stability of a lithium metal battery. The composition of this SEI layer is designed towards employing the coated layer for lithium metal anodes in carbonate-based and ether-based electrolyte systems. This work provides an alternative approach to effectively protect the lithium electrode before cycling in a battery.

1 Introduction

The widespread interest in electrification has increased the necessity for sustainable and effective battery systems now more than ever before. Lithium ion batteries (LIBs) currently hold a large share in the energy storage market and have been successfully employed in most portable consumer electronics, aiding the goal of reaching a carbon-neutral society. However, the energy density of LIBs falls short of meeting some emerging high-power and long-range applications due to limitations in material capacity and design constraints. Based on the traditional intercalation chemistry of graphite anodes, LIBs almost approached their theoretical energy density limit. To overcome this challenge, the lithium metal anode with exceptionally high theoretical specific capacity (3860 mA h g^{-1}) and low negative electrochemical potential (−3.04 V *vs.* standard hydrogen electrode) has been regarded as the ultimate anode candidate for next-generation high energy density batteries.[1–7] Nevertheless, the low electrochemical potential of lithium metal also leads to high reactivity which further causes low cycle stability and typically the formation of lithium dendrites. The safe and efficient utilization of lithium metal remains a challenging yet unavoidable task for widespread lithium metal anode usage.[5,8–10]

Lithium metal stability becomes even more critical when it is being used in more challenging chemistries such as lithium–sulfur (Li–S) batteries. Currently, Li–S cells with high sulfur loading and lean electrolyte conditions reach only a few tens of cycles before the depletion of the Li metal anode and electrolyte by side reactions (*e.g.*, polysulfide shuttle effect) and non-uniform Li deposition.[11–15] It has recently been found that the issues of liquid consumption and dendritic Li plating behavior can be mitigated when traditional liquid electrolytes are replaced by polymer electrolytes.[16–18] However, the use of polymer electrolytes is typically limited by low ionic conductivity, high interfacial resistance, and slower reaction kinetics.[19] Therefore, pretreatments, protective coatings, or artificial solid electrolyte interphases (SEIs) formed through the addition of additives or electrolyte modifications seem to be a feasible approach to enhance Li metal stability.[20–25]

The use of protective coatings that can act as an artificial SEI allows the diffusion of Li ions while reducing the contact area between Li metal and the electrolyte. The protective layer can mitigate the non-uniform deposition of Li metal and therefore the random growth of Li dendrites. Ideally, the artificial protective coating layer on top of the lithium metal should be (1) chemically and electrochemically stable and (2) mechanically flexible and robust to accommodate the volume change during lithium stripping/deposition.[26–28] Based on

General Motors Global Research and Development Center, Warren, MI 48090, USA. E-mail: sanaz.ketabi@gm.com

† Electronic supplementary information (ESI) available. See DOI: https://doi.org/10.1039/d4lf00083h

these requirements, soft polymers have great flexibility to adaptively attach to the lithium surface. However, their low mechanical modulus is not desirable for suppressing lithium dendrite growth. Inorganic components with high mechanical stiffness and high ionic conductivity are good SEI candidates but their inherent brittleness remains a challenge. Hybrid materials come with a combination of organic and inorganic materials that can have the advantages of flexibility and rigidity simultaneously, which offers a promising and viable strategy for making more robust interfaces within the protective film. Therefore, the utilization of an artificial SEI-like coating is a versatile concept that allows the tunability of the coating with organic–inorganic materials to address challenges associated with different battery chemistries.

In comparison with *in situ* coating, the *ex situ* coating method enables us to tune the inorganic component in the artificial SEI layer. Therefore, the rationale behind the selection of pretreatment reagents is critical. The formation of a network of linear polymeric chains that are highly compatible with the Li metal anode can be an ideal framework to incorporate other inorganic materials for protective coatings. 1,3-Dioxolane (DOL), as a cyclic ether, is widely used in Li–S batteries as an electrolyte solvent. It was found that DOL polymerizes on the lithium anode and forms an elastic and ionically conductive stable SEI where formation of $-CH_2CH_2-OCH_2O-Li$ and RCOO–Li segments can improve the lithium cycle stability.[29–31] In this work, a multi-component solution is employed to form a composite artificial SEI layer through solution casting onto the lithium metal anode before cycling. By combining the benefits of DOL with those of other inorganic components, we used ring-opening polymerization of DOL to form a polymer matrix which has great flexibility to adaptively attach to the lithium surface. We also selected Lewis acid salts such as lithium hexafluorophosphate ($LiPF_6$) or lithium difluoro(oxalato)borate (LiDFOB) as a polymerization initiator which can tune the speed and degree of polymerization.[32–35] Different inorganic salts were added into the poly-DOL framework, aiming to improve the Li metal cycle stability through different mechanisms for Li–NMC or Li–S chemistries. Lithium nitrate ($LiNO_3$) is widely used as an electrolyte additive in ether-based electrolytes to stabilize the lithium metal anode. However, due to its low solubility in carbonate-based electrolytes, it had not been extensively used for Li–NMC batteries in the past. As an approach for Li–NMC cells, $LiNO_3$ was incorporated into the artificial SEI layer. With the introduction of $LiNO_3$ into the poly-DOL framework, the N-rich SEI consists of both inorganic species such as LiN_xO_y and organic species such as R–O–Li that can improve the cycling stability.[36–38] In another approach for Li–S cells, lithium bis(trifluoromethane)sulfonimide (LiTFSI) at a high concentration was introduced into the poly-DOL network to create a locally high concentration phase on Li metal that can mitigate side reactions caused by the polysulfide shuttling effect in Li–S batteries. Herein, the effect of the protected Li anode is demonstrated in both carbonate-based and ether-based electrolytes.

2 Experimental section

2.1 Materials

1,3-Dioxolane (DOL), 1,2-dimethoxyethane (DME), lithium bis(trifluoromethane)sulfonimide (LiTFSI), lithium hexafluorophosphate ($LiPF_6$), and lithium tetrafluoroborate ($LiBF_4$) were purchased from Gotion. Trimethyl phosphate (TMP), lithium nitrate ($LiNO_3$), and lithium difluoro(oxalato) borate (LiDFOB) were purchased from Sigma-Aldrich. LiTFSI, $LiBF_4$, $LiPF_6$, $LiNO_3$ and LiDFOB were dried in a vacuum oven at 50 °C for 12 hours to remove moisture. DOL, DME, and TMP were dried before use with 3 Å molecular sieves to obtain a water content of less than 10 ppm (tested by Karl Fischer titration) before usage.

2.2 Lithium protective coating

Coating solution preparation. The coating solution for the poly-DOL layer was prepared using two formulations. For applications with carbonate-based electrolytes, a mixture of DOL and TMP at a volumetric ratio of 5 : 1 was stirred in a vial. Then, 0.8 M $LiNO_3$ was added into the solution and mixed until completely dissolved. Additionally, 0.2 M $LiPF_6$ could be added to the solution as an initiator in the last step. For applications with ether-based electrolytes, 3 M LiTFSI was added to a vial with DOL and mixed thoroughly. Subsequently, 0.14 M $LiBF_4$ or 0.14 M LiDFOB was added to the mixture and stirred until dissolved.

Coating process. While the precursor is still liquid, it was casted on a 100 μm lithium foil that was securely taped onto a copper substrate inside a glovebox with an oxygen and moisture content of less than 0.1 ppm. A doctor blade using a wide gap of 50 μm was used for solution casting. The coated lithium for ether-based electrolyte application was also cured at 60 °C for 1 hour. All the coated lithium electrodes were dried afterwards at room temperature overnight under vacuum before cell assembly.

2.3 Cathode preparation

NMC622 cathodes were prepared by casting slurry containing 95% NMC622, 2 wt% PVDF and 3 wt% SuperP conductive carbon. The slurry was cast on aluminum foil with an areal capacity of 4.4 mA h cm^{-2}.

Carbon–sulfur (C–S) composites were prepared by mixing carbon black powder (Ketjen-Black EC600JD, Nouryon) and sulfur (Sigma-Aldrich) and loading the carbon host *via* melt diffusion at 155 °C for 4 hours. The cathode electrodes were then prepared *via* casting slurry containing 87 wt% C–S composite, 8 wt% multi-walled carbon nanotubes (Cheaptubes) and 5 wt% polyvinylpyrrolidone binder solution (Sigma-Aldrich). The slurry was cast on aluminum foil with an areal active material mass loading of 4.5 mg_S cm^{-2}.

2.4 Material characterization

Coin cell assembly. 2032 coin cells (Hohsen Corp.) were assembled inside a glovebox with an oxygen and moisture level of less than 0.1 ppm. Celgard 2500 polypropylene membranes 19 mm in diameter were used as separators. The carbonate electrolyte was 1 M $LiPF_6$ in diethyl carbonate (DEC)/fluoroethylene carbonate (FEC) (4 : 1). 20 μL electrolyte was used in the Li/Li symmetrical cell with 10 μL on each lithium surface, while 30 μL electrolyte was used for the Li/NMC 622 full cell (4.4 mA h cm^{-2}, 13.5 mm in diameter) with one drop on the lithium surface and the remaining on the cathode. 90 μm thick lithium foil with a copper current collector (12.5 mm in diameter) was used for the lithium symmetrical cell. 30 μm thick lithium foil with a copper current collector (15.6 mm in diameter) was used in the Li–NMC cell.

For ether-based electrolyte applications, 0.6 M LiTFSI and 0.4 M $LiNO_3$ in DME were used. 30 μL electrolyte was used for the Li/Li symmetrical cells, while 40 μL electrolyte (electrolyte : sulfur 8 : 1 μL mg_S^{-1}) was used for the Li/S full cell (13 mm in diameter) with one drop on the lithium surface and the rest on the cathode.

Electrochemical characterization. Symmetrical cells were cycled with a current density of 1 mA cm^{-2} for 4 hours after 6 hours of resting. Li–NMC cells were first rested for 6 hours and then cycled at C/10 for the first two formation cycles, then charged at C/10 and discharged at C/5 for the following cycles. For material screening, full cells were tested at C/3 after two formation cycles at room temperature on a Land CT3001A system. Li–S cells were rested for 2 hours and then cycled at C/20 for the first two formation cycles, and then cycled at C/10 for the following cycles between 1.7 and 2.8 V. Potentiostatic electrochemical impedance spectroscopy (PEIS) was performed using a Biologic VMP3 instrument with a voltage amplitude of 10 mV and frequency ranging from 1 MHz to 1 Hz.

Chemical characterization. Coin cells were disassembled using a Hohsen disassembling tool in a glovebox. The cycled lithium metal electrodes were rinsed with 5 ml dimethyl carbonate (DMC) to remove the residual electrolyte solvent and salt. The morphology of the cycled lithium electrodes was characterized by scanning electron microscopy (SEM, Hitachi S-4800). Lithium cross-sectional images were obtained *via* a Hitachi IM4000 Ar^+ ion milling system with an accelerating voltage of 6 kV and milling for 2 hours. The elements in the coating layer were characterized by energy dispersive X-ray spectroscopy (EDS mapping, Ametek) and analyzed using the Texture and Elemental Analytical Microscopy (TEAM) software. Fourier-transform infrared spectroscopy (FTIR) was performed using a Thermo Nicolet iS10 instrument. X-ray photoelectron spectroscopy (XPS, Thermo Fisher Scientific NEXSA Surface Analyzer) was employed to measure the chemical composition of the coating layer. A monochromated, micro-focused, low power Al Kα X-ray source (1486.6 eV) was used for XPS measurements. A vacuum sample holder was used to transfer the coated lithium metal electrodes from the Ar-filled glovebox to the XPS system to avoid air exposure. The chamber for loading samples was vacuum pumped and achieved $<10^{-6}$ bar before the samples were transferred into the analysis chamber. The analysis chamber was maintained at $<10^{-8}$ bar before analysis. Despite samples being conductive, a flood gun was also used to compensate for the charges. X-ray spot size was set to 400 μm. The data analysis was conducted using Thermo Fisher Avantage software to calculate the relative atomic ratios, identify chemical states and deconvolute the peaks. The molecular weight of poly-DOL gels prepared with different initiators was determined by gel permeation chromatography (GPC, Agilent) against polystyrene standards, using the 1260 Infinity II Multidetector GPC/SEC system. THF was used as an eluent at a flow rate of 1 mL min^{-1} at a temperature of 40 °C. The thermal initiation of poly-DOL was studied by differential scanning calorimetry (DSC, TA instruments). Liquid precursor samples weighing approximately 10 mg were placed in aluminum pans and heated from room temperature to 50 °C, 60 °C and 70 °C at a heating rate of 5 °C min^{-1} and held isothermally for 2 hours under a nitrogen flow of 80 mL min^{-1}.

3 Results and discussion

3.1 Chemical and electrochemical properties of the protective coating layer

The material properties and electrochemical impact of the protective coating or artificial SEI layer were investigated in carbonate-based electrolytes. The polymerization solution consisting of DOL/TMP/$LiNO_3$ was used to form a thin layer coating on lithium. TMP was used as a mixing solvent which can tune the speed of the polymerization reaction of DOL, increase the solubility of $LiNO_3$, and can be reduced to lithiated organic phosphate on the surface of lithium metal.[39–43] The reduction production of $LiNO_3$ and TMP is confined in the poly-DOL matrix to form a N-rich and P-rich SEI layer which can further stabilize the lithium anode stripping and plating behavior.

The morphology of the coating layer was first examined using SEM as shown in Fig. 1. Before plating, the scratch marks shown on the pristine lithium metal in Fig. 1a are due to the manufacturing and cleaning process. The intrinsic oxide layer was gently removed by using a brush inside the glovebox. Fig. 1b shows the lithium surface after being coated with the DOL/TMP/$LiNO_3$ solution, where a smoother surface with the presence of some spherical shapes can be observed. Visually, after DOL/TMP/$LiNO_3$ coating, Li keeps the shiny metallic feature with a thin smooth and sticky layer on top. Several characterization methods are employed to characterize the coating layer. As EDS elemental mapping data of the lithium surface show in Fig. 1e and f, the round clusters in the SEM image are nitrogen- and oxygen-rich. $LiNO_3$ as the only nitrogen source in the coating solution is

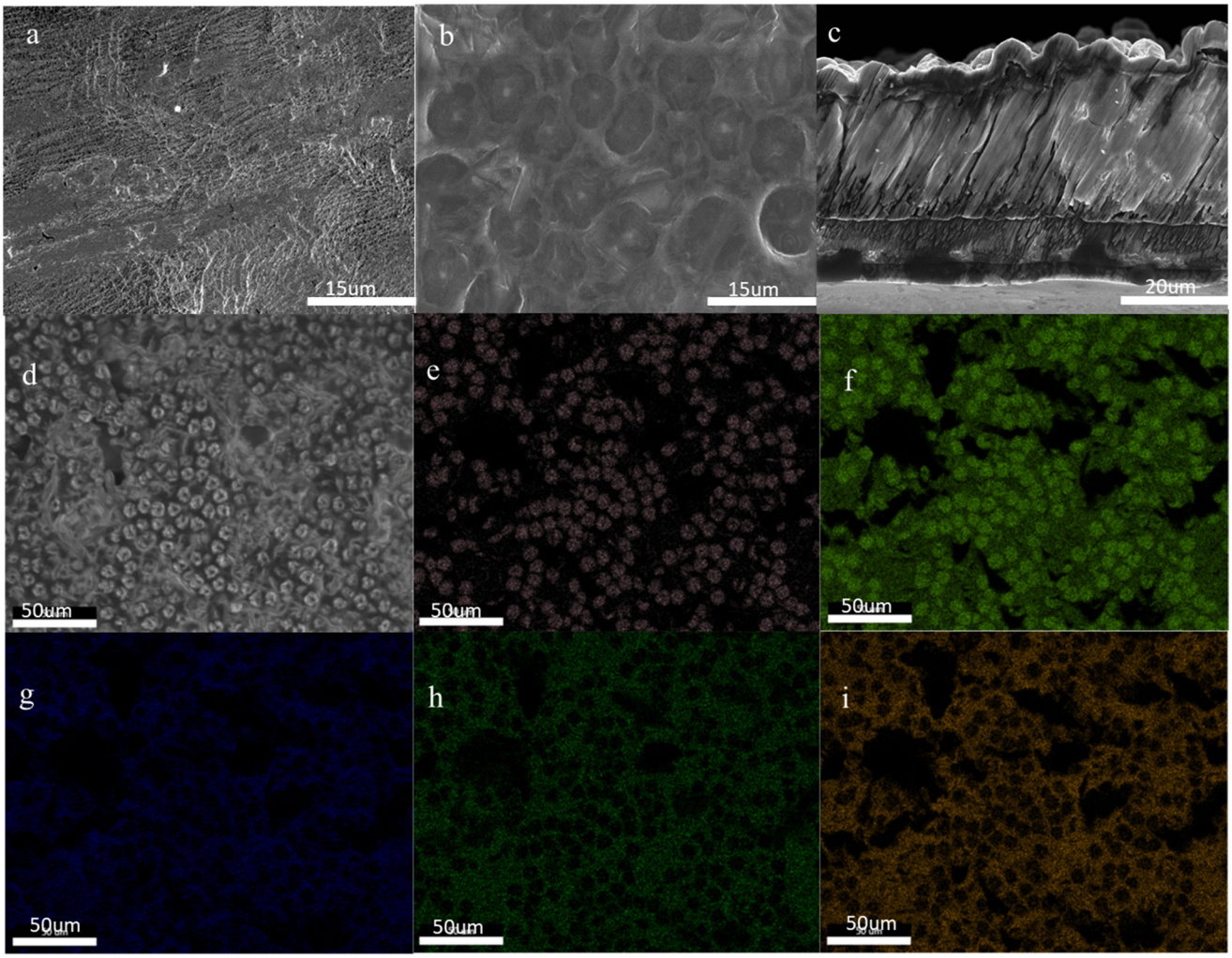

Fig. 1 SEM image of lithium metal electrode showing the morphology comparison between (a) bare lithium without coating before plating and (b) DOL/TMP/$LiNO_3$ coated lithium before plating. (c) Cross section of coated lithium before plating. (d) Top view SEM image of DOL/TMP/$LiNO_3$/1 M $LiPF_6$ coated lithium surface before plating with EDS elemental mapping: (e) nitrogen, (f) oxygen, (g) carbon, (h) phosphorus, (i) fluorine.

shown as round dots in the SEM image. The poly-DOL filler, which confines $LiNO_3$, contains carbon, oxygen and phosphorus as indicated in Fig. 1f and h. To determine the thickness of the coated layer, the cross section of the coated lithium was obtained by ion-milling. The resulting cross-sectional image is observed in Fig. 1c, where the copper substrate is found at the bottom, followed by the lithium metal, and on the top a thin layer corresponding to the hybrid coating layer is noted. The thickness of the coating layer, which adapts to the roughness of the lithium metal surface, is estimated to be about 3–5 μm from the cross section figure.

To have a better understanding of the chemical composition of the coated layer, the coated lithium metal electrode was analyzed by XPS with spectra shown in Fig. 2a and b for N 1s and O 1s, and in Fig. S1† for C 1s and P 2p. The N 1s spectrum reveals that the major component of N in the coating layer is $LiNO_3$ (406.5 eV). Additionally, the peaks located at 403.5 eV and 400.2 eV account for $LiNO_2$ and LiN_xO_y which are reduced from $LiNO_3$. Combining the N 1s spectrum in Fig. 2a with the EDS elemental mapping of nitrogen in Fig. 1e, we can suggest that the crowded round dots shown in Fig. 1b are the $LiNO_3$ from the coating solution together with the reduction products of $LiNO_3$ such as $LiNO_2$ and LiN_xO_y. Such a nitrogen-rich SEI layer has been proven to stabilize the lithium metal electrode surface in the past.[36–38,44,45] Even though $LiNO_3$ is extensively used as an effective electrolyte additive in ether-based electrolytes to improve the stability of lithium metal, it is rarely utilized in carbonate electrolytes due to its low solubility. With $LiNO_3$ confined in the coated artificial SEI, the coating layer acts as a $LiNO_3$ reservoir which can slowly release Li ions into the electrolyte and form a new nitrogen-rich SEI upon lithium cycling. According to the O 1s spectrum in Fig. 2b, most of the oxygen in the coating layer is identified as polyether with a peak located at 534 eV. As a cyclic ether, the reduction of DOL on lithium had been studied.[46] It can also explain why a thin, smooth, and sticky layer is formed on lithium. The

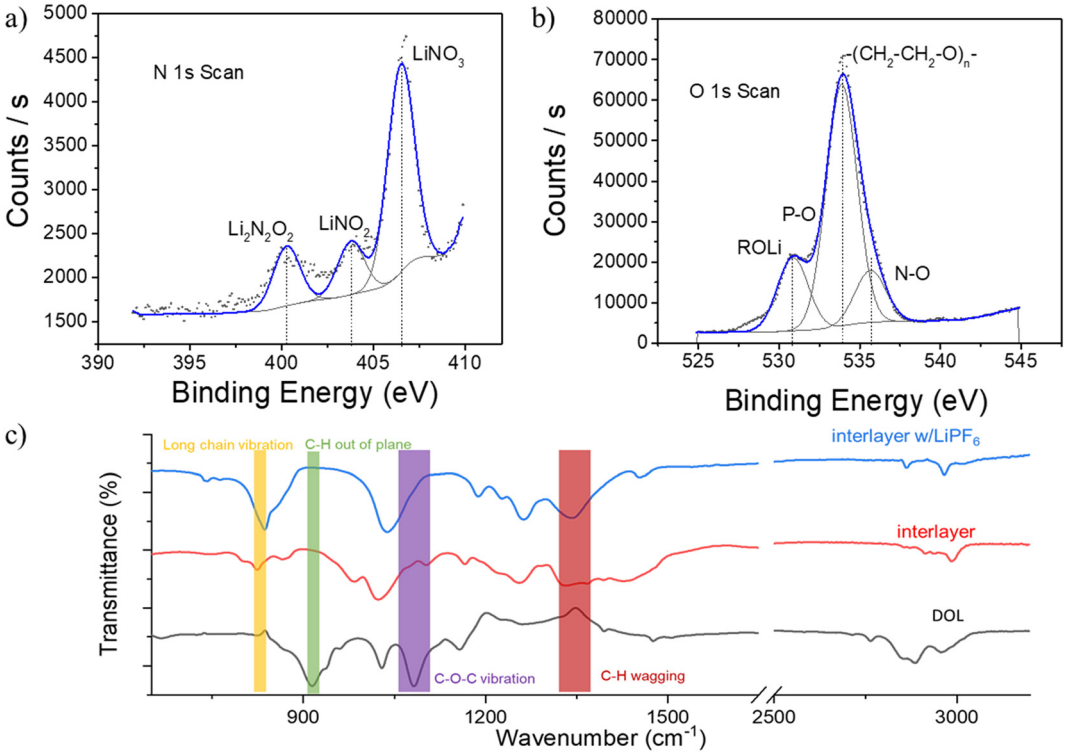

Fig. 2 XPS spectra of DOL/TMP/$LiNO_3$/1 M $LiPF_6$ coated layer. (a) N 1s spectrum, (b) O 1s spectrum. (c) FTIR spectroscopy of DOL and interlayer coated lithium electrode.

oxygen-rich layer in Fig. 1f is also confirmed by EDS mapping. Besides the O in $LiNO_3$, O can also be found in the confinement around the $LiNO_3$. These O atoms come from the poly-DOL, which suggests a matrix covering the lithium metal surface and confining a great amount of $LiNO_3$. Additionally, as observed in Fig. S1,† there is a clear peak at 286.5 eV in the C 1s spectra, confirming the presence of polymer carbon chains.

FTIR spectroscopy analysis was performed to further support the formation of poly-DOL. Pure DOL solvent and lithium after DOL/TMP/$LiNO_3$ coating were tested and compared. As shown in Fig. 2c, the FTIR spectra of the coated layer or interlayer involve particular peaks that are different from those of DOL which are highlighted with color bars and are assigned to the basic structure of poly-DOL. A new C–H wagging vibration at 1350 cm^{-1} for the interlayer

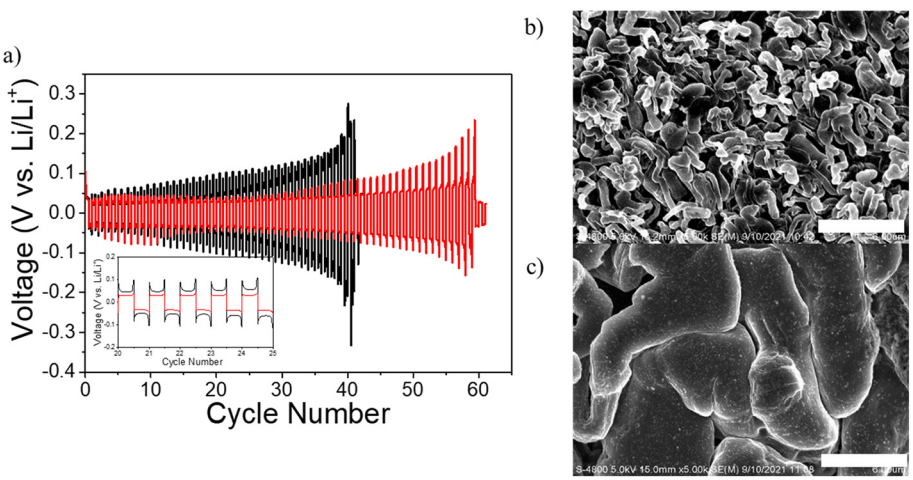

Fig. 3 (a) Representative voltage profile of symmetrical cells using lithium without (black) and with (red) poly-DOL coating layer. Inset: enlarged portion of the voltage profile between cycles 20 and 25. Top view SEM image of lithium metal electrode. Morphology comparison after areal capacity of 4 mA h cm^{-2} lithium plated (b) bare lithium, (c) DOL/TMP/$LiNO_3$ coated lithium. The scale bar represents 6 μm.

spectra appears. The disappearance of C–O–C vibration at 1082 cm^{-1} indicates the ring opening of DOL. The disappearance of C–H out of plane at 918.5 cm^{-1} and the appearance of long-chain vibration at 850 cm^{-1} indicate the polymerization of DOL.

Symmetrical configuration cells were assembled to investigate the impact of the poly-DOL coating layer on the electrochemical performance of lithium metal electrodes. The testing parameters were selected to resemble full cell operating conditions with NMC electrodes. In symmetrical cells, where lithium ions originated from the lithium metal itself, with an areal capacity of 4 mA h cm^{-2} (theoretically equivalent to 20 μm lithium), lithium was plated and stripped in each cycle at 1 mA cm^{-2} current density (Fig. 3a). The electrolyte/capacity ratio was 4 mL A h^{-1} for coin cells. Considering the 90 μm lithium electrode used in symmetrical cells, close to 25% of lithium was involved in each cycle which is high enough to quickly reveal the effect of coating on the Li electrode in this harsh electrochemical testing.

After plating of 4 mA h cm^{-2} lithium, the structure and morphology of Li deposition were characterized with SEM as shown in Fig. 3b and c. Without the coating layer, lithium is deposited as a needle or dendritic structure with a diameter less than 1 μm as shown in Fig. 3b. Such a mossy lithium growth leads to a larger surface area. More fresh lithium was exposed to the electrolyte and formed excess SEI by side reaction, which accelerated the irreversible loss of electrolyte and lithium. With further cycling, more dead lithium was formed, which increased Li ion diffusion tortuosity, and the plating–stripping overpotential increased as shown in Fig. 3a. The increasing overpotential is due to the stripping of lithium from the bulk lithium through the dead lithium and excess SEI layer, and the plating of lithium onto the SEI and dead lithium. Fig. 3c presents the morphology of lithium deposition with a DOL/TMP/$LiNO_3$ coating layer, which shows a significantly different lithium plating pattern in much larger pieces with diameters larger than 3 μm. Denser lithium deposition will certainly lead to less volume expansion and less side reaction as well as less lithium and electrolyte loss upon cycling. Compared to the porous deposition of bare lithium after 20 cycles in Fig. 3b, the coating layer can also survive long-term cycling, resulting in a dense and uniform lithium surface as shown in Fig. 3c.

The deposition–stripping overpotential continues to increase with more cycling until a sudden drop in overpotential caused by the internal short of the Li/Li cell. As shown in Fig. 3a, the symmetrical cell using bare lithium metal electrode can complete only 42 cycles before the sudden drop in overpotential. Meanwhile, the coating layer can increase the cycle life by 42.8% with up to 60 cycles before overpotential dropping. The inset of Fig. 3a shows the electrochemical potential profile of galvanostatic stripping and deposition of Li. Coated Li shows lower stripping and plating overpotential. The different overpotentials clearly originate from the passivation layer on bare Li electrode caused by the formation of extra SEI. The sudden drop in overpotential may account for the repeatedly increasing mechanical strain on the separator imposed by the growing volume of the Li electrode, ultimately resulting in the breach of the separator and subsequent internal shorting of the battery.

Based on the discussed analyses, the designed *ex situ* hybrid organic and inorganic interlayer was confirmed to be formed on the lithium metal surface by simultaneous polymerization of DOL and incorporation of inorganic nitrate and phosphate components. The developed artificial SEI is the poly-DOL matrix which provides a robust and flexible polymer matrix to confine other components as an interlayer. All these components can work together to protect the Li metal anode and improve Li cycle stability. In the following sections, the impact of the coated Li on the electrochemical performance of the full cell is discussed. To investigate the effects of coated lithium with different electrolytes, we first explored the performance of Li–NMC622 full cells with carbonate electrolytes. Then, the composition of the coated layer was modified to demonstrate the compatibility and performance of lithium–sulfur cells with protected Li anode using ether-based electrolytes.

3.2 Li metal protection in Li–NMC

Full cells were assembled with bare and coated Li metal anode and NMC622 cathode. As shown in Fig. 4a, cells with coated lithium electrodes show higher initial discharge capacity than those with bare lithium. It is attributed to the decrease in cell impedance for the cells with a coating layer as shown in Fig. 4b. The cell impedance of coated lithium (R_{total} = 88 ohm) is lower than that of bare lithium (R_{total} = 103 ohm). A smaller impedance value translates to lower overpotential in galvanostatic cell cycling. As shown in black in Fig. 4a, cells with bare lithium show drastic capacity decay after 80 cycles. However, in the initial 100 cycles, a more stable cycle life can be achieved with the protection of the coating layer. After around 100–120 cycles, the discharge capacity of the cell with coated Li suddenly dropped.

A possible reason for the failure mechanism could be that the confined $LiNO_3$ in the coating layer has been completely consumed after 100 cycles. The total amount of $LiNO_3$ is limited in the coating layer. It slowly dissolves into electrolyte and continues to react with fresh lithium in each cycle. It can be reduced to LiN_xO_y or even Li_3N. Although the reduced products can also promote the cycle stability, they cannot play the same important role as that of $LiNO_3$ in the SEI. During the reduction reaction of $LiNO_3$, lithium is also consumed by the redox side reaction which will clearly deteriorate cell performance. Another reason for $LiNO_3$ consumption could be the formation of gas upon cell cycling.[47] This can be proved with post-mortem chemical characterization in future investigations.

Thin polymer coatings cannot tolerate repeated large volume changes and could cause fracture in the layer, or they can detach from the lithium surface. Therefore, a higher

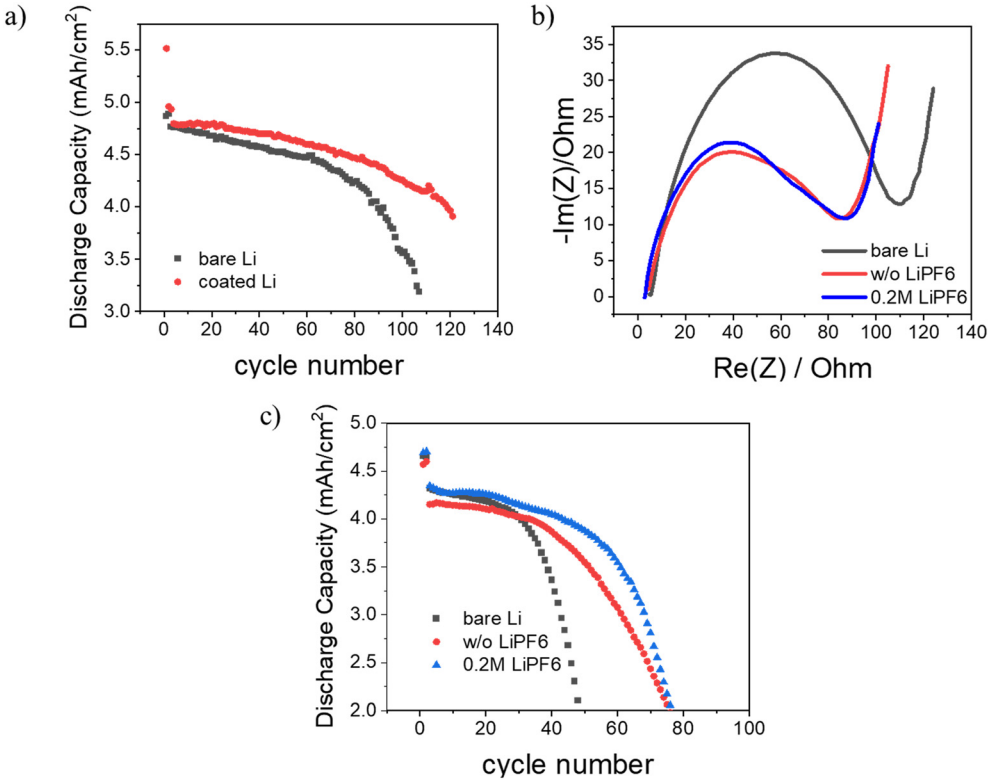

Fig. 4 (a) Areal discharge capacity as a function of cycle number for Li–NMC622 cells with bare lithium (black squares) and poly-DOL/TMP/$LiNO_3$ coated lithium (red circles). (b) Nyquist plot of Li–NMC622 cells with bare lithium (black), coated lithium with no initiator (red) and with 0.2 M $LiPF_6$ as initiator (blue). (c) Areal discharge capacity as a function of cycle number for Li–NMC622 cells with bare lithium (black squares), poly-DOL/TMP/$LiNO_3$ coated lithium (red circles), and poly-DOL/TMP/$LiNO_3$ with 0.2 M $LiPF_6$ initiator coated lithium (blue triangles).

degree of polymerization might improve the mechanical integrity of the polymer layer. The incorporation of a polymerization initiator into the organic–inorganic composite artificial SEI layer can tune the polymerization degree and thickness of the poly-DOL interlayer. $LiPF_6$ is a commonly used weakly coordinated lithium salt in carbonate-based electrolytes. Moreover, $LiPF_6$ has a spontaneous decomposition reaction to form LiF and PF_5.[48–50] PF_5 is a Lewis acid initiator which can further break the C–O bond in DOL and initiate a ring-opening chain reaction. Thus, we proposed the addition of small amounts of $LiPF_6$ salt to act as a ring-opening initiator and tune the mechanical properties of the hybrid interlayer. The FTIR analysis shown in Fig. 2c confirmed that the addition of $LiPF_6$ in the coating solution could strengthen the polymerization, indicated by the larger peak in long-chain vibration regions.

To study the effects of the ring-opening initiator on the formation of the coating layer and consequently on the cell performance, coating solutions with varying concentrations of $LiPF_6$ were prepared and the coated lithium were tested in full cell configurations. The stability of DOL/TMP/$LiNO_3$ coated lithium was examined with a higher current density of 2.1 mA (C/3) after two formation cycles. 30 μm lithium metal anodes, NMC622 cathode electrodes with an areal capacity of 4.4 mA h cm^{-2}, and 30 μL electrolyte were used for each cell. As seen in Fig. 4c, the DOL/TMP/$LiNO_3$ coated lithium electrodes show better capacity retention than bare lithium. This is consistent with the cycle performance mentioned in Fig. 4a. The DOL/TMP/$LiNO_3$ multi-component solution can build an artificial SEI layer to stabilize lithium in plating/stripping cycling. The degradation of cell performance is slowed down by the coating layer. However, the $LiNO_3$ consumption and poly-DOL degradation would deteriorate the stability of the protective layer over long cycles. With the introduction of the initiator into the coating solution, more DOL will be polymerized on the lithium surface, resulting in a thicker polymer matrix to confine more $LiNO_3$ and Li_3PO_4, leading to less cell impedance. Fig. 4b and c show that with the addition of 0.2 M $LiPF_6$ to the coating solution the cell impedance decreased in comparison to that of bare lithium and the cell performance improved, retaining a higher capacity.

However, further increase in the concentration of $LiPF_6$ above 0.5 M did not show significant improvement in capacity retention and the resulting thick coating layer led to higher cell impedance as observed in Fig. S3.† The thick coating layer increases charge transfer impedance as well as mass transfer impedance, even though it contains $LiNO_3$ intended to improve ionic conductivity.

An inhomogeneous coating layer causes nonuniform local current distribution and results in mossy porous lithium growth. In addition, the viscous coating solution also makes

it difficult to completely dry the coating layer. The residual solvent might contaminate the electrolyte, and residual DOL is not stable at high electrochemical potentials. A high content of $LiPF_6$ is also not desirable as it can react with trace amounts of moisture in the electrolyte and form HF, which is proven to be detrimental for cell performance.[51,52] These drawbacks led us to investigate other initiators which could induce ring-opening of DOL while being moderate initiators and compatible with electrolyte. We also altered the chemical composition of the coating layer, aiming at demonstrating the performance of coated lithium in ether-based electrolytes with sulfur cathode which is discussed in the following section.

3.3 Li metal protection in Li–S

Lewis acids such as $LiBF_4$ and LiDFOB are also promising salts used in lithium-ion batteries which can act as an initiator to induce the cationic ring-opening reaction of cyclic ethers like DOL. GPC was utilized to study the effect of each initiator on the chain length of linear poly-DOL under varied conditions. The polymerization process of the precursor solution consisting of DOL/3 M LiTFSI/0.14 M initiator was carried out in both a closed environment and an open environment where the effects of monomer concentration could be studied. This was done by placing the liquid precursor in both a tightly closed vial and a vial with an untight cap placed on top which we will refer to as "closed vial" and "open vial", respectively. The effect of temperature on the polymerization process was also investigated by heating the precursor solution after the initiator addition. A summary of the measured molecular weight of the different poly-DOL samples is presented in Fig. 5a. The results indicate that the chain size of poly-DOL is much larger when the polymerization is carried out in a closed environment, regardless of the initiator. At room temperature, $LiBF_4$ leads to longer poly-DOL chain size which is consistent with our observation where a liquid precursor could fully polymerize in a short time. To resemble the solution casting process, the open cap polymerization at 60 °C shows that adding LiDFOB to the coating solution results in a slightly higher molecular weight. LiDFOB is a moderate initiator compared to $LiBF_4$ and therefore allows for chain growth for a longer time. These results provide further understanding of the differences in chain length of the resulting polymers when considering an *ex situ* coating process on the lithium surface.

Thermal analysis was conducted to optimize the poly-DOL coating processing conditions. Fig. 5b shows DSC thermograms of DOL/LiTFSI/LiDFOB used as precursor coating solution at different heating temperatures. The exothermic peak represents the heat generation during polymerization. The time required to complete the polymerization decreased with increasing temperature. However, it seems that 60 °C would be an optimum heating temperature during the solution casting process where the polymerization of DOL monomers can proceed as shown by GPC analysis.

The stability of lithium coated with poly-DOL/LiTFSI/LiDFOB was examined in ether-based electrolyte for application in Li–S battery. The anticipated functions of the coating layer are as a protective layer for lithium and a barrier which delays polysulfide diffusion and side reaction with lithium metal. The impact of the poly-DOL coating on Li cycling stability was first investigated in symmetrical cells. To verify the impact of the polymer phase on impeding polysulfide diffusion, DOL was eliminated from the standard liquid electrolyte (0.6 M LiTFSI + 0.4 M $LiNO_3$ in DME), preventing its possible polymerization during cell cycling and testing its performance under harsher conditions. As shown in Fig. S4,† the cell with Li anode coating shows a similar Li plating/stripping profile to the cell without coating at early cycles which continues with a stable voltage profile. However, the cell without coating shows an increase in cell polarization, indicating a non-uniform Li stripping/plating during cycling.

Since Li metal cycling in ether electrolyte was promising, we investigated the feasibility and cycling stability of coated Li in Li–S full cells. Fig. 6 shows the voltage profiles and cycle life of Li–S cells with and without poly-DOL coated lithium. As expected, the Li–S cell with uncoated Li anode in the DME

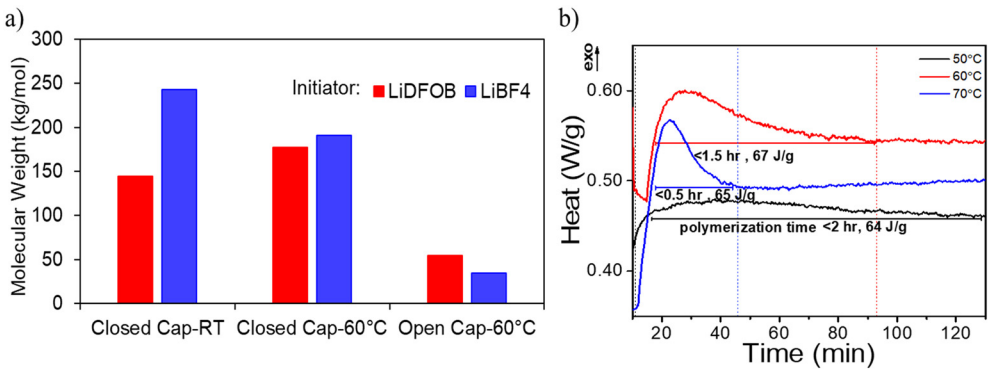

Fig. 5 (a) Molecular weight of poly-DOL using LiDFOB (red) and $LiBF_4$ (blue) as initiators determined by GPC. (b) DSC thermograms of coating solution using LiDFOB as initiator, from room temperature to 50, 60, and 70 °C at a heating rate of 5 °C min^{-1}.

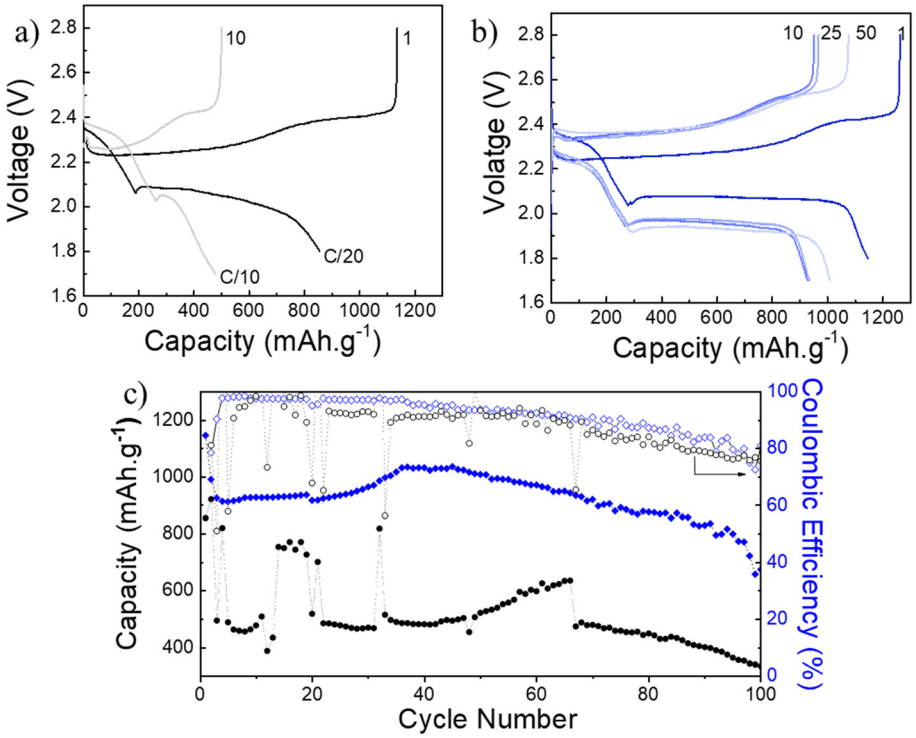

Fig. 6 Electrochemical performance of Li–S cells using (a) bare lithium, (b) poly-DOL/LiTFSI/LiDFOB coated lithium. (c) Cycling stability and coulombic efficiency of Li–S cells with bare lithium (black) and poly-DOL/LiTFSI/LiDFOB coated lithium (blue) at a current density of 100 mA g^{-1}.

liquid electrolyte showed poor electrochemical performance (Fig. 6a), where the capacity rapidly decayed after the 3rd cycle due to the depletion of Li metal anode and electrolyte due to side reactions with polysulfides. In contrast, significantly higher specific capacity, a complete second potential plateau, and prolonged cycle life was observed for cells with coated Li anode (Fig. 6b). This suggests that hybrid organic–inorganic coating layers are effective in impeding the side reactions of polysulfides with Li anode. The high concentration of LiTFSI salt in the poly-DOL network could create local areas of low solubility for polysulfides to diffuse. The cycling performances of Li–S cells using bare and coated Li are compared in Fig. 6c, where the cells with coated Li anode achieved much higher specific capacity with an improved capacity retention reaching 800 mA h g^{-1} at 100 cycles and coulombic efficiency over 80%. These results demonstrated that the poly-DOL coatings developed through an *ex situ* method effectively performed as a protective layer for the Li anode. The cycling performance of cells with coated Li significantly outperformed cells with bare Li, even when DOL is eliminated from the standard electrolyte.

After 100 cycles, cells with coated Li showed a gradual decay in capacity which could be due to the increase in the concentration of polysulfides generated during cycling and reaction with lithium metal. To obtain insight into the stability of the coated layer, Li metal anodes were retrieved from Li–S coin cells with and without a protective coating layer at the end of life, and the surface morphology was examined using SEM and EDS. Fig. 7a shows the cross section SEM image of fresh Li metal with coating layer. The thickness of the coating layer is non-uniform which could be due to the surface morphology of the Li metal surface or the variation in polymer system chain structure. The SEM images of the Li surface without and with a protective coating after cycling are shown in Fig. 7b and c, respectively. As expected, the Li surface shows a mossy structure with dead Li and reaction products with polysulfides. However, areas of unreacted Li, which can be seen in Fig. 7c, might suggest that this intact portion of Li metal was not involved in electrochemical reaction. EDS mapping on this area supports our observation where traces of S are negligible on the intact areas of Li metal (Fig. 7d). These analyses suggest that while the coating layer was able to protect Li metal, the polymer system composition and coating process require modification to achieve a homogenous thickness that can lead to uniform Li plating/stripping.

4 Conclusion

In our study, we have successfully developed an organic–inorganic hybrid coating layer on the surface of lithium to protect it upon cycling. A polymerized DOL framework was selected as an organic component due to its elasticity and good compatibility towards Li. Different organic salts were used for different cathode and electrolyte systems. The long cycle stability data show that such an organic–inorganic hybrid coating layer can regulate Li stripping and deposition behavior and protect Li upon cycling. However, there are still

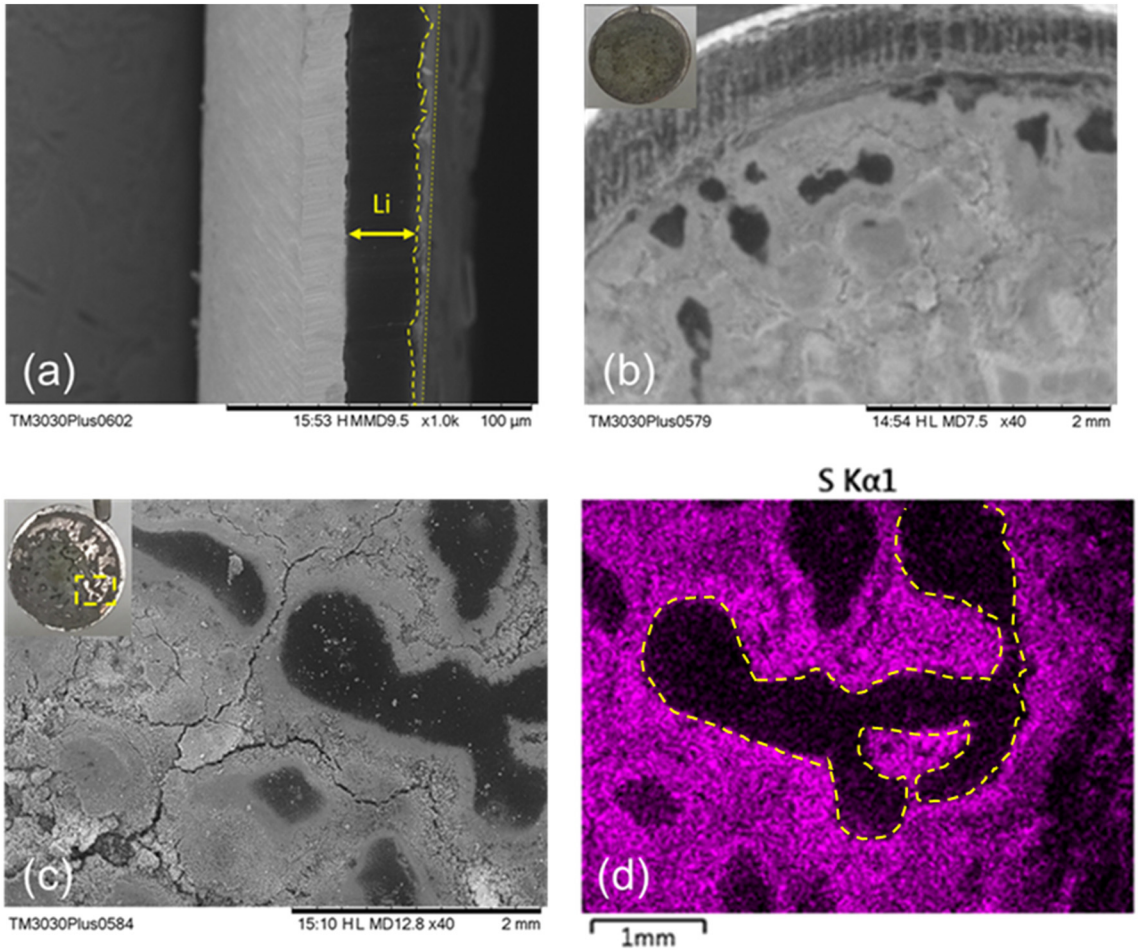

Fig. 7 (a) Cross section SEM image of fresh Li with coating layer. Top view SEM image of Li surface (b) without and (c) with poly-DOL/LiTFSI/LiDFOB coating layer at the end of life. (d) Corresponding EDS mapping analysis of Li with coating layer showing S elemental distribution.

some challenges for this hybrid coating layer. First, the non-uniformity of the *ex situ* coated layer can result in an uneven Li ion flux, leading to early cell failure. Poly-DOL will also swell and slowly dissolve into the electrolyte system as shown in Fig. S5† with ether-based electrolyte. This will further promote the non-uniformity of the coating layer. Modified polymerization time and temperature with optimized concentration of polymerization initiator might improve the structural stability of the coating layer. Another challenge is that the inorganic salt included in the coating layer will dissolve and be consumed throughout cycling. Further investigation and modification using solvents with different solubility properties are needed to overcome these issues.

Conflicts of interest

There are no conflicts of interest to declare.

Acknowledgements

SK, MF and FD are grateful for the financial support of DOE Battery500 Consortium, award DE-EE0008230. YZ and XX acknowledge the funding of the Department of Energy (DOE) award DE-EE0008863.

References

1 X.-B. Cheng, R. Zhang, C.-Z. Zhao and Q. Zhang, *Chem. Rev.*, 2017, **117**, 10403–10473.
2 J. Li, Z. Kong, X. Liu, B. Zheng, Q. H. Fan, E. Garratt, T. Schuelke, K. Wang, H. Xu and H. Jin, *InfoMat*, 2021, **3**, 1333–1363.
3 X. He, D. Bresser, S. Passerini, F. Baakes, U. Krewer, J. Lopez, C. T. Mallia, Y. Shao-Horn, I. Cekic-Laskovic, S. Wiemers-Meyer, F. A. Soto, V. Ponce, J. M. Seminario, P. B. Balbuena, H. Jia, W. Xu, Y. Xu, C. Wang, B. Horstmann, R. Amine, C.-C. Su, J. Shi, K. Amine, M. Winter, A. Latz and R. Kostecki, *Nat. Rev. Mater.*, 2021, **6**, 1036–1052.
4 B. Horstmann, J. Shi, R. Amine, M. Werres, X. He, H. Jia, F. Hausen, I. Cekic-Laskovic, S. Wiemers-Meyer, J. Lopez, D. Galvez-Aranda, F. Baakes, D. Bresser, C.-C. Su, Y. Xu, W. Xu, P. Jakes, R.-A. Eichel, E. Figgemeier, U. Krewer, J. M. Seminario, P. B. Balbuena, C. Wang, S. Passerini, Y. Shao-Horn, M. Winter, K. Amine, R. Kostecki and A. Latz, *Energy Environ. Sci.*, 2021, **14**, 5289–5314.

5 J. Zhang, J. Shi, X. Wen, Y. Zhao and J. Guo, *ACS Appl. Mater. Interfaces*, 2020, **12**, 32863–32870.
6 W. Xu, J. Wang, F. Ding, X. Chen, E. Nasybulin, Y. Zhang and J.-G. Zhang, *Energy Environ. Sci.*, 2014, **7**, 513–537.
7 Y. Zhao and J. Guo, *InfoMat*, 2020, **2**, 866–878.
8 B. Liu, J.-G. Zhang and W. Xu, *Joule*, 2018, **2**, 833–845.
9 A. Varzi, K. Thanner, R. Scipioni, D. Di Lecce, J. Hassoun, S. Dörfler, H. Altheus, S. Kaskel, C. Prehal and S. A. Freunberger, *J. Power Sources*, 2020, **480**, 228803.
10 J. Zhang, M. Zhou, J. Shi, Y. Zhao, X. Wen, C.-C. Su, J. Wu and J. Guo, *Nano Energy*, 2021, **88**, 106298.
11 A. Manthiram, Y. Fu and Y.-S. Su, *Acc. Chem. Res.*, 2013, **46**, 1125–1134.
12 Y. V. Mikhaylik and J. R. Akridge, *J. Electrochem. Soc.*, 2004, **151**, A1969.
13 Y.-X. Yin, S. Xin, Y.-G. Guo and L.-J. Wan, *Angew. Chem., Int. Ed.*, 2013, **52**, 13186–13200.
14 S.-E. Cheon, K.-S. Ko, J.-H. Cho, S.-W. Kim, E.-Y. Chin and H.-T. Kim, *J. Electrochem. Soc.*, 2003, **150**, A796.
15 Y. Zhao, J. Zhang and J. Guo, *ACS Appl. Mater. Interfaces*, 2021, **13**, 31749–31755.
16 G. G. Eshetu, X. Judez, C. Li, M. Martinez-Ibañez, I. Gracia, O. Bondarchuk, J. Carrasco, L. M. Rodriguez-Martinez, H. Zhang and M. Armand, *J. Am. Chem. Soc.*, 2018, **140**, 9921–9933.
17 R. Xu, J. Yue, S. Liu, J. Tu, F. Han, P. Liu and C. Wang, *ACS Energy Lett.*, 2019, **4**, 1073–1079.
18 X. Judez, H. Zhang, C. Li, G. G. Eshetu, J. A. González-Marcos, M. Armand and L. M. Rodriguez-Martinez, *J. Electrochem. Soc.*, 2018, **165**, A6008.
19 C. Shen, J. Xie, M. Zhang, P. Andrei, M. Hendrickson, E. J. Plichta and J. P. Zheng, *Electrochim. Acta*, 2017, **248**, 90–97.
20 N. Akhtar, X. Sun, M. Yasir Akram, F. Zaman, W. Wang, A. Wang, L. Chen, H. Zhang, Y. Guan and Y. Huang, *J. Energy Chem.*, 2021, **52**, 310–317.
21 Q. Jin, K. Zhao and X. Zhang, *J. Power Sources*, 2021, **489**, 229500.
22 G. Zheng, C. Wang, A. Pei, J. Lopez, F. Shi, Z. Chen, A. D. Sendek, H.-W. Lee, Z. Lu, H. Schneider, M. M. Safont-Sempere, S. Chu, Z. Bao and Y. Cui, *ACS Energy Lett.*, 2016, **1**, 1247–1255.
23 Q. Jin, K. Zhao, J. Wang, J. Xiao, L. Wu, X. Zhang, L. Kong, L. Li, H. Lu, Y. Xie, W. Li and X. Zhang, *ACS Appl. Mater. Interfaces*, 2022, **14**, 53850–53859.
24 C. Huang, J. Xiao, Y. Shao, J. Zheng, W. D. Bennett, D. Lu, L. V. Saraf, M. Engelhard, L. Ji, J. Zhang, X. Li, G. L. Graff and J. Liu, *Nat. Commun.*, 2014, **5**, 3015.
25 Y. M. Lee, N.-S. Choi, J. H. Park and J.-K. Park, *J. Power Sources*, 2003, **119–121**, 964–972.
26 H. Wang, Y. Liu, Y. Li and Y. Cui, *Electrochem. Energy Rev.*, 2019, **2**, 509–517.
27 Y. Liu, D. Lin, P. Y. Yuen, K. Liu, J. Xie, R. H. Dauskardt and Y. Cui, *Adv. Mater.*, 2017, **29**, 1605531.
28 R. Xu, X.-B. Cheng, C. Yan, X.-Q. Zhang, Y. Xiao, C.-Z. Zhao, J.-Q. Huang and Q. Zhang, *Matter*, 2019, **1**, 317–344.
29 D. Aurbach, O. Youngman and P. Dan, *Electrochim. Acta*, 1990, **35**, 639–655.
30 Y. Gofer, Y. Ein Ely and D. Aurbach, *Electrochim. Acta*, 1992, **37**, 1897–1899.
31 Y. Zhao, X. Xiao, S. Chen and M. Cai, *US Pat.*, 17578169, 2023.
32 M. Xie, Y. Wu, Y. Liu, P. P. Yu, R. Jia, W. A. Goddard and T. Cheng, *Mater. Today Energy*, 2021, **21**, 100730.
33 J. L. Goldman, L. A. Dominey and V. R. Koch, *J. Power Sources*, 1989, **26**, 519–523.
34 K. Khan, Z. Tu, Q. Zhao, C. Zhao and L. A. Archer, *Chem. Mater.*, 2019, **31**, 8466–8472.
35 H. Wu, B. Tang, X. Du, J. Zhang, X. Yu, Y. Wang, J. Ma, Q. Zhou, J. Zhao, S. Dong, G. Xu, J. Zhang, H. Xu, G. Cui and L. Chen, *Adv. Sci.*, 2020, **7**, 2003370.
36 J. Guo, Z. Wen, M. Wu, J. Jin and Y. Liu, *Electrochem. Commun.*, 2015, **51**, 59–63.
37 Z. Wang, K. Yang, Y. Song, H. Lin, K. Li, Y. Cui, L. Yang and F. Pan, *Nano Res.*, 2020, **13**, 2431–2437.
38 D. W. Kang, J. Moon, H.-Y. Choi, H.-C. Shin and B. G. Kim, *J. Power Sources*, 2021, **490**, 229504.
39 Z. L. Brown, S. Heiskanen and B. L. Lucht, *J. Electrochem. Soc.*, 2019, **166**, A2523.
40 H. Ota, A. Kominato, W.-J. Chun, E. Yasukawa and S. Kasuya, *J. Power Sources*, 2003, **119–121**, 393–398.
41 P. Shi, H. Zheng, X. Liang, Y. Sun, S. Cheng, C. Chen and H. Xiang, *Chem. Commun.*, 2018, **54**, 4453–4456.
42 X. Wang, E. Yasukawa and S. Kasuya, *J. Electrochem. Soc.*, 2001, **148**, A1058.
43 L. Zhang, Y. Huang, H. Fan and H. Wang, *ACS Appl. Energy Mater.*, 2019, **2**, 1363–1370.
44 M. Liu, Z. Cheng, K. Qian, T. Verhallen, C. Wang and M. Wagemaker, *Chem. Mater.*, 2019, **31**, 4564–4574.
45 I. Phiri, J. Kim, D.-H. Oh, M. Ravi, H.-S. Bae, J. Hong, S. Kim, Y.-C. Jeong, Y. M. Lee, Y.-G. Lee and M.-H. Ryou, *ACS Appl. Mater. Interfaces*, 2021, **13**, 31605–31613.
46 Q. Liu, A. Cresce, M. Schroeder, K. Xu, D. Mu, B. Wu, L. Shi and F. Wu, *Energy Storage Mater.*, 2019, **17**, 366–373.
47 A. Jozwiuk, B. B. Berkes, T. Weiß, H. Sommer, J. Janek and T. Brezesinski, *Energy Environ. Sci.*, 2016, **9**, 2603–2608.
48 T. Kawamura, S. Okada and J.-i. Yamaki, *J. Power Sources*, 2006, **156**, 547–554.
49 C. L. Campion, W. Li and B. L. Lucht, *J. Electrochem. Soc.*, 2005, **152**, A2327.
50 A. Guéguen, D. Streich, M. He, M. Mendez, F. F. Chesneau, P. Novák and E. J. Berg, *J. Electrochem. Soc.*, 2016, **163**, A1095.
51 K. Tasaki, K. Kanda, S. Nakamura and M. Ue, *J. Electrochem. Soc.*, 2003, **150**, A1628.
52 J.-w. Liu, X.-h. Li, Z.-x. Wang, H.-j. Guo, W.-j. Peng, Y.-h. Zhang and Q.-y. Hu, *Trans. Nonferrous Met. Soc. China*, 2010, **20**, 344–348.